Numerical integration methods in gas-bubble dynamics

Vinod Kamath and Andrea Prosperetti

Department of Mechanical Engineering, The Johns Hopkins University, Baltimore, Maryland 21218

A recent detailed formulation of the dynamics of a gas bubble requires the numerical integration of a nonlinear heat equation in the bubble. In this article, a variety of numerical methods for this purpose are studied. The most efficient technique is found to be an adaptive Galerkin–Chebyshev spectral method, which is explained in detail. Examples of oscillations at high forcing and chaotic response are also given. These results differ very considerably from those obtained by use of the simpler models used by previous investigators.

PACS numbers: 43.35.Ei, 43.25.Yw, 43.30.Nb

INTRODUCTION

A detailed mathematical model for the internal thermo-fluid mechanics of a gas bubble has been developed by Nigmatulin and co-workers[1-3] and by Prosperetti et al.[4] In Ref. 4, it was compared with the common, less sophisticated polytropic approaches (see, e.g., Refs. 5–9), and very significant discrepancies between the two results were found in so many cases that the reliability of the common approach in situations other than the simplest ones appears seriously questionable. For example, an effort to study the chaotic behavior of driven bubble oscillations[10,11] or the propagation of pressure waves in bubbly liquids[12,13] in terms of this model cannot be expected to give results with better than order-of-magnitude accuracy.

Unfortunately, the new model requires the solution of a nonlinear heat equation inside the bubble and is, therefore, considerably more demanding computationally than older ones. It is, therefore, important to develop simple and efficient numerical techniques. This is the objective we pursue in the present article. We compare the finite-difference technique of Ref. 4 with a number of spectral methods. The best technique that we find offers an order-of-magnitude improvement over the finite-difference approach. To facilitate the use of this technique, we give detailed explanations and formulas in the Appendix. As an example of its applications, we show a Poincaré plot of a chaotic attractor and a bifurcation diagram for a bubble oscillating under the action of a slowly growing pressure amplitude. Very significant differences are found between these results and those obtained with the simpler models used by previous investigators.

I. THE MODEL

The radial dynamics of a bubble of radius $R(t)$ in a compressible liquid is described by Keller's equation[14-16]

$$\left(1 - \frac{\dot{R}}{c}\right)R\ddot{R} + \frac{3}{2}\left(1 - \frac{\dot{R}}{3c}\right)\dot{R}^2$$
$$= \frac{1}{\rho_L}\left(1 + \frac{\dot{R}}{c} + \frac{R}{c}\frac{d}{dt}\right)[p_B - p_A(t)], \tag{1}$$

where the overdots denote time differentiation, ρ_L is the liquid density, c is the speed of sound, p_A is the "ambient" pressure, and p_B is the pressure in the liquid just outside the bubble. The precise definition of p_A is the pressure at the

bubble center in the absence of the bubble,[14,16] but, if the scale for the spatial change of this quantity is much larger than the bubble radius, $p_A(t)$ also very nearly equals the liquid pressure far from the bubble. The pressure p_B is related to the pressure in the bubble by the condition on the normal stresses at the interface

$$p = p_B + 2\sigma/R + 4\mu_L(\dot{R}/R), \tag{2}$$

where p is the internal pressure, σ is the surface tension coefficient, and μ_L is the liquid viscosity. For the cases to be considered in this article, the ambient pressure $p_A(t)$ is a given function of time and the following, slightly modified, form of the radial equation is more convenient:

$$\left(1 - \frac{\dot{R}}{c}\right)R\ddot{R} + \frac{3}{2}\left(1 - \frac{\dot{R}}{3c}\right)\dot{R}^2$$
$$= \frac{1}{\rho_L}\left(1 + \frac{\dot{R}}{c} + \frac{R}{c}\frac{d}{dt}\right)p_B - \frac{1}{\rho_L}\left(1 + \frac{\dot{R}}{c}\right)p_A\left(t + \frac{R}{c}\right). \tag{3}$$

The central point of the new model is the calculation of the internal pressure with the assumption of spatial uniformity of this quantity and perfect gas behavior of the bubble contents. It is shown in Ref. 4 that, with these assumptions, from the enthalpy equation of the gas in conservation form, the following expression for the radial velocity of the gas in the bubble readily follows:

$$u = \frac{1}{\gamma p}\left((\gamma - 1)K\frac{\partial T}{\partial r} - \frac{1}{3}r\dot{p}\right). \tag{4}$$

Here, γ is the ratio of the specific heats of the gas, K is the thermal conductivity, T is the temperature, and r is the distance from the bubble's center. By evaluating this expression at the bubble wall, where $u = \dot{R}$, and solving for $\dot{p}$, one finds

$$\dot{p} = \frac{3}{R}\left((\gamma - 1)K\frac{\partial T}{\partial r}\Big|_R - \gamma p\dot{R}\right), \tag{5}$$

which is an equation for the internal pressure. To close the problem, an equation for the temperature is needed. In view of the way in which (5) was derived, one can use either the enthalpy equation in nonconservation form or the equation of continuity coupled with the equation of state of perfect gases. The first alternative leads to

$$\frac{\gamma}{\gamma-1}\frac{p}{T}\left[\frac{\partial T}{\partial t}+\frac{1}{\gamma p}\left((\gamma-1)K\frac{\partial T}{\partial r}-\frac{1}{3}r\dot{p}\right)\frac{\partial T}{\partial r}\right]-\dot{p}$$
$$=\nabla\cdot(K\nabla T). \qquad (6)$$

In Ref. 4, it is also shown that, in relatively "cold" liquids, such as water at normal ambient temperature, the exact boundary condition can be approximated by the simpler one

$$T[r=R(t),t]=T_{\infty}, \qquad (7)$$

where T_{∞} is the undisturbed liquid temperature.

For numerical work, it is convenient to deal with a fixed spatial integration domain and we therefore use the new variable

$$y=r/R(t). \qquad (8)$$

Furthermore, to account more easily for the variability of the gas thermal conductivity, we introduce the new dependent variable

$$\tau=\int_{T_{\infty}}^{T}K(\theta)d\theta. \qquad (9)$$

The linear relation $K(T)=AT+B$ with $A=5.528$ erg/cm s °K^2 and $B=1165$ erg/cm s °K gives a good fit to the thermal conductivity of air in the range $200\,K<T<3000$ °K. Finally, it is also useful to deal with quantities nondimensionalized as follows:

$$R=R_0R_*, \quad t=t_*/\omega, \quad p=p_0p_*, \quad T=T_{\infty}T_*,$$
$$\tau=D_0p_0\tau_*, \quad D=D_0D_*. \qquad (10)$$

Here, R_0 and p_0 are the values of the radius and internal pressure at equilibrium and are connected by

$$p_0=2\sigma/R_0+p_{\infty}, \qquad (11)$$

where p_{∞} is the static pressure, ω is a typical inverse time (e.g., the frequency of the sound field driving the bubble into oscillation), and D_0 is the equilibrium value of the thermal diffusivity given, for a perfect gas, by

$$D=[(\gamma-1)/\gamma]\,[K(T)T/p]. \qquad (12)$$

In terms of these variables, the pressure and temperature equations (5) and (6) become, omitting asterisks,

$$p'=\frac{3}{R}\left(\frac{\gamma-1}{R}\chi\frac{\partial\tau}{\partial y}\bigg|_{y=1}-\gamma pU\right), \qquad (13)$$

$$\frac{\partial\tau}{\partial t}+\frac{\gamma-1}{\gamma}\frac{\chi}{pR^2}\left(\frac{\partial\tau}{\partial y}-\frac{\partial\tau}{\partial y}\bigg|_{y=1}y\right)\frac{\partial\tau}{\partial y}-Dp'$$
$$=\frac{\chi D}{R^2}\nabla^2\tau, \qquad (14)$$

where primes denote differentiation with respect to the dimensionless time and

$$U=R'. \qquad (15)$$

The parameter χ is defined by

$$\chi=D_0/\omega R_0^2 \qquad (16)$$

and is the square of the ratio of the diffusion length to the equilibrium radius. In terms of τ, the boundary condition (7) is

$$\tau(1,t)=0. \qquad (17)$$

With the linear relation used for the thermal conductivity, the dimensionless temperature T expressed in terms of τ is

$$T=(1/\alpha)\{[1+2[(\gamma-1)/\gamma]\alpha\tau]^{1/2}+\alpha-1\} \qquad (18)$$

and

$$D=(1/p)[\alpha T^2+(1-\alpha)T], \qquad (19)$$

where $\alpha=AT_{\infty}/K(T_{\infty})$.

Upon substitution of (2) and (10), and omitting asterisks, the radial equation (3) becomes

$$\left(1-\frac{U}{c_*}+\frac{ZM}{Rc_*}\right)RU'+\frac{3}{2}\left(1-\frac{U}{3c_*}-\frac{2ZM}{3Rc_*}\right)U^2$$
$$=Z\left\{\left(1+\frac{U}{c_*}\right)\left[p-p_A\left(t+\frac{R}{c_*}\right)-\frac{W+MU}{R}\right]\right.$$
$$\left.+\frac{R}{c_*}\left(p'+\frac{WU}{R^2}\right)\right\}, \qquad (20)$$

where

$$Z=\frac{p_0}{\rho_L\omega^2R_0^2},$$
$$W=\frac{2\sigma}{R_0p_0}, \quad M=\frac{4\mu_L\omega}{p_0}, \quad c_*=\frac{c}{\omega R_0}. \qquad (21)$$

The total mass of gas contained in the bubble is given in dimensionless units by

$$m=3pR^3\int_0^1\frac{y^2}{T}dy. \qquad (22)$$

We have found that the deviation of this quantity from 1, which is the exact value, gives a reliable indication of the accuracy of the calculation.

A finite-difference, second-order, predictor–corrector method for the solution of (13), (14), and (20) was described in detail in Ref. 4 and will not be repeated. In the following sections, we shall only consider some spectral methods applied to the approximation of the spatial operators appearing in Eqs. (13) and (14). Since the use of such methods in fluid mechanics is so well documented in papers and books, only a brief description is necessary here. For more details, the reader may consult Refs. 17 and 18. For the time integration of the resulting system of ordinary differential equations, use has been made of the standard subroutine DGEAR with Gear's stiff method of order 6.

II. GALERKIN METHOD

To apply the Galerkin spectral method, we approximate the temperaturelike field τ by its projection onto the N-dimensional manifold spanned by suitable basis functions $\phi_n, n=1,2,...,N$. If P_N is the projection operator onto this manifold, we have $\tau_N=P_N\tau$ or, more explicitly,

$$\tau_N=\sum_{k=1}^{N}a_k(t)\phi_k(y). \qquad (23)$$

Once the basis functions ϕ_k are selected, the problem is thus reduced to the determination of the time dependence of the coefficients a_k of this expansion. For this purpose, use is made of the energy equation (14).

As basis functions, we use the shifted Chebyshev polynomials

$$\phi_n = T_{2n} - T_0, \tag{24}$$

which ensure satisfaction of the boundary condition (17) at the bubble wall. Since polynomials of even order are even functions of y, this choice also satisfies $\partial \tau / \partial y = 0$ at the bubble center. A minor disadvantage of the use of (24) is that these functions are not orthogonal. Explicit expressions for the scalar products (ϕ_k, ϕ_n) are given in the Appendix.

To apply the Galerkin method, the energy equation is projected in succession on the basis functions $\phi_1, \phi_2, \ldots$ by taking the scalar products

$$\left(\phi_k, \frac{\partial \tau_N}{\partial t} \right) = (\phi_k, \mathsf{N}(\tau_N))$$
$$+ \frac{\gamma - 1}{\gamma} \frac{\chi}{pR^2} \frac{\partial \tau_N}{\partial y} \bigg|_{y=1} (\phi_k, \mathsf{L}\tau_N), \tag{25}$$

with $k = 1, 2, \ldots$. In writing this equation, we have broken up the spatial operator in (14) into a linear part

$$\mathsf{L}\tau_N = y \frac{\partial \tau_N}{\partial y} \tag{26}$$

and a nonlinear part

$$\mathsf{N}(\tau_N) = \frac{\chi}{R^2} \left[D(\tau_N) \nabla^2 \tau_N - \frac{\gamma - 1}{\gamma p} \left(\frac{\partial \tau_N}{\partial y} \right)^2 \right]$$
$$+ D(\tau_N) p'. \tag{27}$$

It is easy to show that

$$\nabla^2 \tau_N = \sum_{n=0}^{N} d_n T_{2n}, \tag{28}$$

$$\frac{\partial \tau_N}{\partial y} = \sum_{n=1}^{N} e_n T_{2n-1}, \tag{29}$$

where the coefficients d_n and e_n are given in the Appendix. In view of the complicated dependence of D on τ the integration implicit in the scalar product $(\phi_k, \mathsf{N}(\tau_N))$ must, however, be performed numerically. For this purpose, we use the formula

$$(\phi_k, \mathsf{N}(\tau_N)) = 2 \sum_{j=1}^{N} w_j \phi_k(y_j)$$
$$\times \left\{ \frac{\chi}{R^2} \left[D[\tau_N(y_j)] (\nabla^2 \tau_N)|_{y_j} \right. \right.$$
$$\left. \left. - \frac{\gamma - 1}{\gamma p} \left(\frac{\partial \tau_N}{\partial y} \right)^2 \bigg|_{y_j} \right] + D[\tau_N(y_j)] p' \right\}, \tag{30}$$

where the w_j's and y_j's are the appropriate weights and zeros for Gauss integration also given in the Appendix. The other scalar product $(\phi_k, \mathsf{L}\tau_N)$ involving the linear term can be calculated analytically as shown in the Appendix. We also tested the use of a Gauss–Lobatto, rather than Gauss, integration, but found negligible differences. Another concern in the numerical integration arises because of possible aliasing errors. We have addressed this point by using $3N/2$ and $2N$ quadrature points rather than N and have found the formula (30) to be free from significant aliasing errors.[18] The extra

accuracy thus gained in the integration does not have any effect even when a small number of terms, such as 4 or 5, is used.

With the previous procedure, the energy equation (14) is reduced to

$$\sum_{n=1}^{N} (\phi_k, \phi_n) \frac{da_n}{dt} = (\phi_k, \mathsf{N}(\tau_N))$$
$$+ \frac{\gamma - 1}{\gamma} \frac{\chi}{pR^2} \frac{\partial \tau_N}{\partial y} \bigg|_{y=1} (\phi_k, \mathsf{L}\tau_N), \tag{31}$$

for $k = 1, 2, \ldots, N$, where the right-hand side is calculated as explained. This is a linear algebraic system for the time derivatives of the expansion coefficients da_k/dt, which is solved by LU-decomposition (or explicitly, as shown in the Appendix) to yield values for these quantities. With the above manipulations, the partial differential equation is reduced to a system of ordinary differential equations that can be integrated in time.

It will be seen from the numerical results that, during a large fraction of each period of oscillation, the motion is relatively slow and the temperature profiles sufficiently mild to require only a few terms in the expansion (23). In the neighborhood of the minima of the radius, on the other hand, velocities are high and the temperature field more severely distorted. This observation has motivated us to try a variant of the Galerkin method that improves efficiency and that consists in the use of a variable number of terms in the expansion (23). This idea is implemented as follows. The coefficient of the last term retained in (23) is compared with the coefficient of the first term. If the ratio of the two is larger than some small number ϵ_A (typically 10^{-4}), another term is added and the parameter N increased by one unit in all the previous relations. The initial value of the coefficient a_{N+1} for the next time step is taken to vanish. If, on the other hand, the ratio is smaller than another preset small number ϵ_D (typically 10^{-6}), the last term of the series is discarded and N decreased by one. Since, to improve efficiency, all the coefficients appearing in relations such as (30) are calculated once at the beginning of the program, in the case of a variable number of terms, it is necessary to calculate and store sets of coefficients corresponding to several values of N, from the minimum allowed value up to the maximum one. In all cases, the number of terms retained was not allowed to fall below 4 or 5.

A most welcome, and unexpected, feature of the Galerkin method described is that the error in the mass contained in the bubble calculated according to (22) does not accumulate in time even with the use of only a small number of terms in the expansion. This is in marked contrast with the finite-difference method of Ref. 4, for which the slowly growing error prevented integration over too many cycles unless an extremely small time step was used.

III. COLLOCATION METHOD

For the collocation method, we still approximate τ by its projection on a finite-dimensional manifold,

$$\tau \simeq \tau_N = \sum_{k=0}^{N} a_k(t)\phi_k(y). \tag{32}$$

Rather than using the shifted Chebyshev polynomials (24) as in the previous Galerkin method, it is computationally slightly more advantageous to use the polynomials directly; i.e., $\phi_k = T_{2k}$. As before, the boundary condition at the bubble center is automatically satisfied by the use of only even polynomials. Now, the ordinary differential equations for the expansion coefficients a_k are obtained by requiring the energy equation (14) to be satisfied exactly at a number of collocation points y_j

$$\sum_{k=0}^{N} \phi_k(y_j)\frac{da_k}{dt} = \left(N(\tau_N)\right.$$
$$\left. + \frac{\gamma-1}{\gamma}\frac{\chi}{pR^2}\frac{\partial\tau_N}{\partial y}\bigg|_{y=1} L\tau_N\right)_{y_j}. \tag{33}$$

If the collocation points are taken to be the Gauss–Lobatto quadrature points,

$$y_j = \cos(\pi j/N), \quad 0 \leqslant j \leqslant N,$$

the boundary point $y = 1$ is a member of the set, and, here, rather than imposing (33), we require

$$\sum_{k=0}^{N} \frac{da_k}{dt}\phi_k(1) = 0, \tag{34}$$

in agreement with the boundary condition (17). Note that $T_{2k}(1) = 1$ for all k.

IV. NUMERICAL RESULTS

We shall now discuss several examples of the application of the methods described previously. Specifically, we consider (1) the adaptive Galerkin method with a variable number of terms, (2) the Galerkin method with a fixed number of terms, (3) the collocation method, and (4) the finite-difference method of Ref. 4. The most precise and efficient of these approaches is the first one, and it is against this method that the other ones will be compared. Our objective in the present study is more to explore the accuracy and efficiency of the different methods than to show specific results of interest in bubble dynamics. Therefore, we shall consider a limited number of cases. In all the examples shown, the driving pressure field is taken as

$$p_A(t) = p_\infty(1 - \epsilon\sin\omega t), \tag{35}$$

which, in the dimensionless variables (10) becomes, upon using ω to nondimensionalize the time,

$$p_{A*}(t) = (1 - W)(1 - \epsilon\sin t_*). \tag{36}$$

Two of the examples used in Ref. 4 were for bubble radii of 10 and 50 μm driven with $\epsilon = 0.6$ at a frequency $\omega/\omega_0 = 0.8$. Here, ω_0 is the resonance frequency of linear theory, and $\omega_0/2\pi = 302.42$ kHz for the 10-μm bubble, while $\omega_0/2\pi = 62.204$ kHz for the 50-μm bubble. These are the two cases we consider. The most direct effect of the calculation of the temperature field in the bubble is on the internal

pressure, and, therefore, we shall focus on this quantity rather than on the bubble radius that, being dependent of the second integral of p, is not as sensitive to the accuracy with which the pressure is calculated.

Figure 1 shows on a semilogarithmic plot the internal pressure during the 20th (external) pressure cycle for the 10-μm case. The calculation was started with $R(0) = 1$, $U(0) = 0$, $T(r,0) = 1$, and it appeared that, by this time, the motion had settled down into steady state. This result was obtained by use of the adaptive Galerkin method with a maximum of 20 terms (i.e., since only even polynomials are used, up to and including T_{40}). The criterion used for the addition of new terms was $\epsilon_A = 10^{-4}$, and that for the deletion of terms was $\epsilon_D = 10^{-6}$. The prominent feature of this result is the high pressure maximum, the position and magnitude of which are sensitive indicators of numerical accuracy. For this reason we shall show detailed comparisons of the peak structure rather than of the complete 20th pressure cycle. The maximum mass error occurred at the peak and was less than 1%. All the results to be discussed are accurate enough that, on a graph such as that of Fig. 1, they would essentially superpose and look identical. The times quoted are for the total duration of the program including the preliminary calculations and the integration for 20 pressure cycles. The integration time for a single cycle can be estimated to vary between 1 and 2.5 min,depending on the accuracy.

In Fig. 2, we show convergence of the finite-difference calculation. Here, and in the following figures, the solid line is the previous Galerkin result. The dotted line is the finite-difference result with 401 internal nodes and 4000 time steps per cycle, and the dashed line is the finite-difference result with 201 nodes and 2000 time steps. Convergence toward the Galerkin result as the discretization is refined is clear here. The two finite-difference calculations took 8.9 and 2.3 h of CPU time on a MicroVax II, while the Galerkin spectral calculation took 0.90 h. The superiority of the spectral method is therefore quite apparent. In Fig. 3, a similar comparison is shown for the Galerkin method with a fixed number of
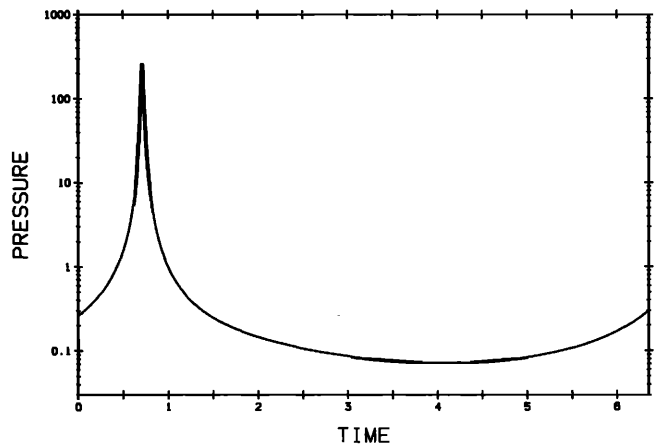

FIG. 1. Internal pressure versus time during the 20th cycle of the driving pressure for a 10-μm-radius air bubble in water driven at $\omega/\omega_0 = 0.8$ with a dimensionless pressure amplitude $\epsilon = 0.6$. By this time, steady state has essentially been reached. The calculation has been performed with the adaptive 20-term Galerkin–Chebyshev expansion described in the text.
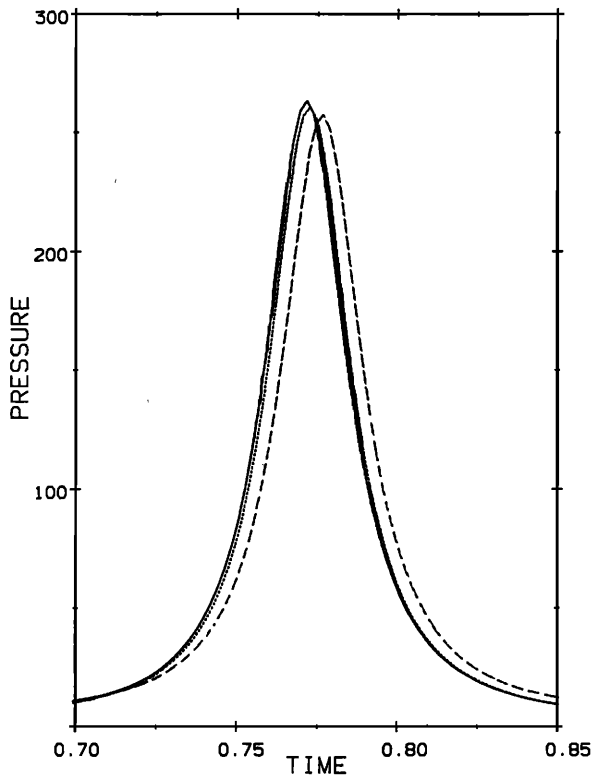
FIG. 2. Comparison of the peak structure of Fig. 1 as given by the adaptive 20-term Galerkin–Chebyshev method (solid line) and two finite-difference calculations. The dotted line has been obtained with 401 internal nodes and 4000 time steps per cycle, the dashed line with 201 nodes and 2000 time steps.
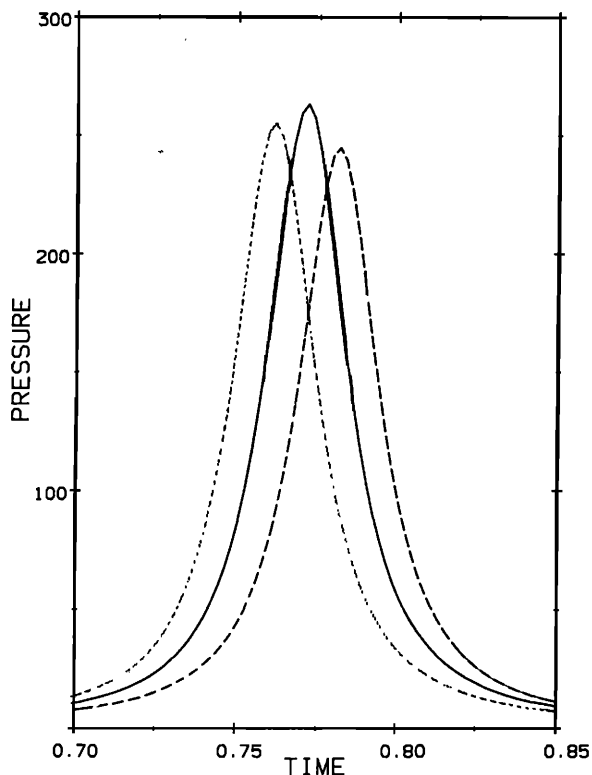
terms, 4 for the dashed line and 6 for the dotted line. The 4-term result gives a 13% error in the height of the peak and a 0.5% error in its position and takes 5 min. The corresponding errors for the 6-term result are 5% and 0.2%, respectively, with an integration time of 20 min. In Fig. 4, the dotted and dashed lines have been obtained with a variable number of terms up to 10 and 7, respectively, with $\epsilon_A = 10^{-4}$, $\epsilon_D = 10^{-6}$, while the dash-and-dot line has been obtained with a maximum of 10 terms but a coarser criterion for the deletion and addition of terms, $\epsilon_A = 10^{-3}$ and $\epsilon_D = 10^{-5}$. Compared with the precise 20-term variable calculation (solid line), the 7-term result has an error of 0.4% in the position of the peak and 1% in its level, but requires only 18 min. This is less than the time required for the fixed 6-term calculation of Fig. 3 and the error is quite comparable. The results shown in these two figures imply that the numerical method is very robust and that its performance deteriorates only slightly with the use of coarser procedures, which, however, lead to substantial savings of computing time. The 10-term calculations of Fig. 4 required 42 and 20 min, respectively. The small difference in computing time between the 20-term (54 min) and the 10-term calculations is also interesting. It implies that extra terms are added during only a small fraction of the cycle, near the radius minimum. To illustrate this, we superpose, in Fig. 5, the number of terms used in the calculation with the pressure, both as functions of time. It is seen that the algorithm used to add and discard terms causes some oscillations in the number of terms used,

FIG. 3. Comparison of the peak structure of Fig. 1 as given by the adaptive 20-term Galerkin–Chebyshev method (solid line), and the fixed 4-term (dashed line) and 6-term (dotted line) Galerkin–Chebyshev integrations.
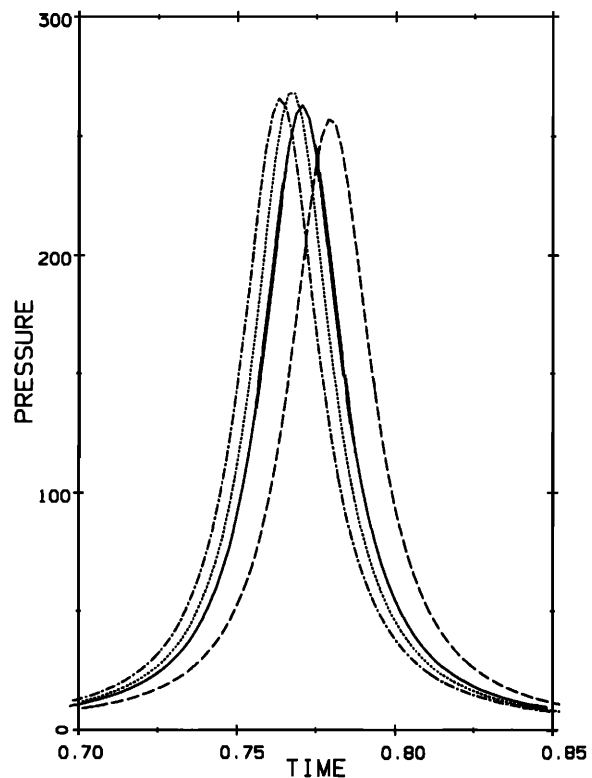

FIG. 4. Comparison of the peak structure of Fig. 1 as given by the adaptive 20-term (solid line), 10-term (dotted line), and 7-term (dashed line) Galerkin–Chebyshev method with $\epsilon_A = 10^{-4}$, $\epsilon_D = 10^{-6}$, and a variable 10-term calculation with $\epsilon_A = 10^{-3}$, $\epsilon_D = 10^{-5}$ (dash-and-dot line).
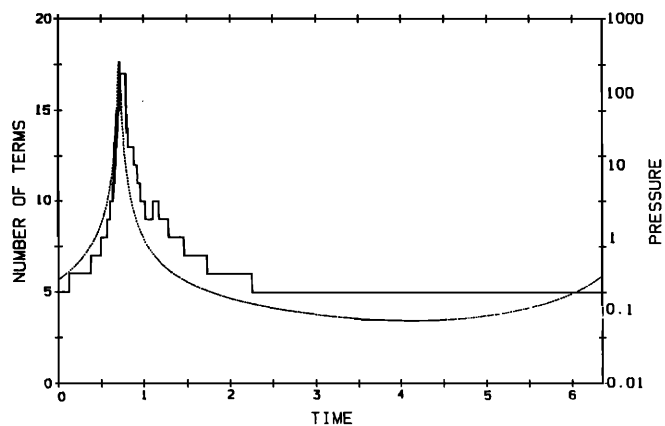
FIG. 5. The number of terms retained in the adaptive 20-term Galerkin calculation is shown here superposed on the pressure-time curve of Fig. 1.

but this is a minor problem that does not affect the accuracy of the calculation but only, in a very minor way, its efficiency. The number of terms retained was not allowed to fall below 5, and it can be seen that, for a substantial fraction of the cycle, 5 terms are quite sufficient. To explore the effect of the tolerance with which terms are added and discarded, we ran the same case with $\epsilon_A = 10^{-5}$ and $\epsilon_D = 10^{-7}$. This more precise calculation took about twice as much as the other one, 1.7 h, but the differences were found to be exceedingly small, 0.4% in the height of the peak and 0.1% in its position.

Another set of comparisons is shown in Figs. 6 and 7 between the 20-term adaptive Galerkin method (solid line)

and some collocation results. The first figure shows convergence of the collocation method with 8 collocation points (dotted line) and 12 collocation points (dashed line). These calculations required 45 and 95 min, respectively. Therefore, the 12-point calculation takes about 50% longer than the 20-term Galerkin calculation, but does not perform nearly as well. Figure 7 shows the adaptive 20-term Galerkin result (solid line) compared with a fixed 6-term Galerkin calculation (dotted line, 20 min), and a 6-point collocation (dashed line, 24 min). The conclusion to be drawn from these results is that the Galerkin method performs much better for a similar computational effort.

In many applications, such as some rectified diffusion calculations, one is interested in nonlinear oscillations of only moderate amplitude. In these applications, one would like to use a simple and fast integration procedure and it is, therefore, important to enquire about the limits of validity of a low-order method. Our experience is that a Galerkin method with 4 terms for a 10-μm bubble driven with $\epsilon = 0.5$ at $\omega/\omega_0 = 0.8$ performs very well, while at higher amplitudes more terms are needed. The same result has been found in other cases, and it therefore seems that a simple 4-term expansion has sufficient accuracy to be widely applicable. We give a detailed description of this method in the Appendix. As in all of these calculations, it is prudent to monitor the total mass in the bubble by evaluating the integral (22) several times during the cycle. A mass loss or gain in excess of a
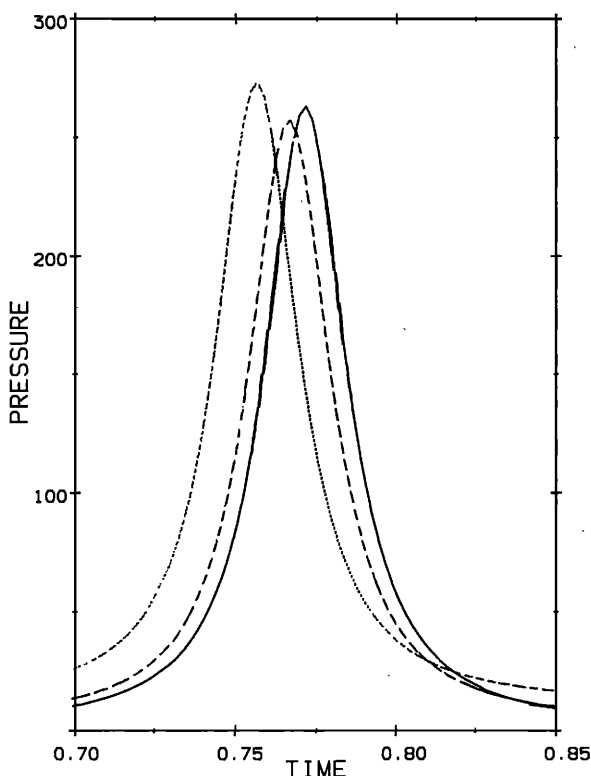

FIG. 6. Comparison of the peak structure of Fig. 1 as given by the adaptive 20-term Galerkin–Chebyshev method (solid line) with the 8-term (dotted line) and 12-term (dashed line) collocation results.
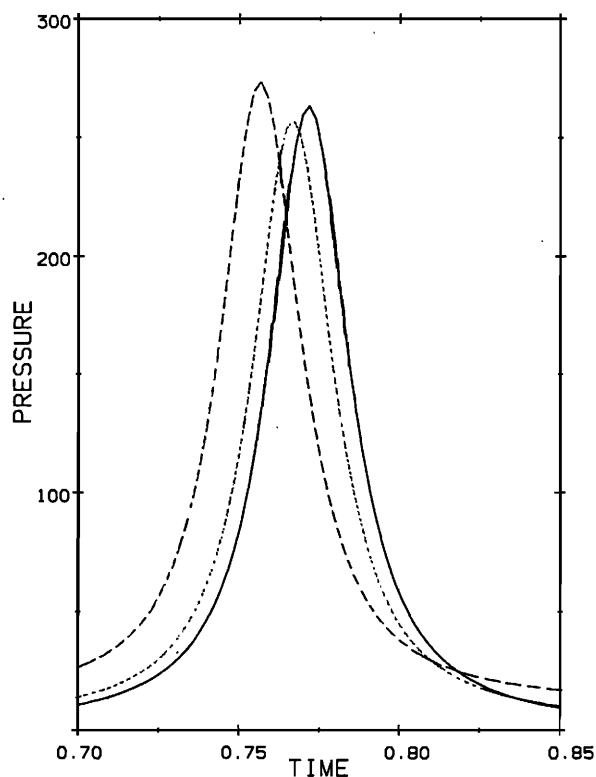

FIG. 7. Comparison of the peak structure of Fig. 1 as given by the variable 20-term Galerkin–Chebyshev method (solid line) with the fixed 6-term Galerkin–Chebyshev method (dotted line) and the 6-term collocation method (dashed line).

few percent is an indication that an insufficient number of terms have been retained in the expansion.

It is interesting to see to what amplitude the present numerical technique can be pushed. We have tested the adaptive 20-term Galerkin method with a forcing $\epsilon = 2.05$ for a 50-μm bubble driven at $\omega/\omega_0 = 0.8$ and found no integration difficulties in reaching steady state after 30 pressure cycles. This result is shown in Fig. 8, in which a subharmonic response is seen with four cycles of the driving pressure for one complete oscillation. A similar finite-difference calculation, which requires 401 nodes and 6000 time steps per pressure cycle, takes about 16 h, to be compared with the 2 h for the one shown. As discussed in Ref. 4, the mathematical model of Sec. I is expected to break down when the Mach number of the bubble wall motion calculated with respect to the speed of sound in the gas approaches 1. During the oscillation shown in Fig. 8, the maximum Mach number with respect to the liquid velocity of sound is somewhat less than 0.1. Since near the minimum radius the temperature in the gas increases by a factor close to four times the undisturbed temperature, this gives a gas Mach number of the order of 0.25, which, although not very small, should result in an error of the order of 10% or less. It should be stressed that all existing models suffer from the same problem at high radial velocities and our model, if anything, can be expected to be less limited than others in this respect. Therefore, although quite numerous in the literature, results obtained at too high a level of forcing are necessarily rather speculative. In Ref. 16, for high-amplitude oscillations, the use of a form of the Keller equation (3), based on the liquid enthalpy rather than the pressure, was advocated. In dimensional form, this equation is

$$\left(1 - \frac{\dot{R}}{c}\right)R\ddot{R} + \frac{3}{2}\left(1 - \frac{\dot{R}}{3c}\right)\dot{R}^2$$
$$= \left(1 + \frac{\dot{R}}{c} + \frac{R}{c}\frac{d}{dt}\right)h_B - \frac{1}{\rho_L}\left(1 + \frac{\dot{R}}{c}\right)p_A\left(t + \frac{R}{c}\right),$$

(37)

where h_B denotes the liquid enthalpy calculated for the value p_B of the pressure just outside the bubble given by (2). For water, one can use the following equation of state:

$$(p + \Gamma)/(p_\infty + \Gamma) = (\rho/\rho_\infty)^n,$$

(38)

where $\Gamma = 3049.13$ bars and $n = 7.15$, to find

$$h = (c^2 - c_\infty^2)/(n - 1),$$

(39)

with the speed of sound c given by

$$c^2 = [n(p + \Gamma)/\rho].$$

In all these relations, the subscript ∞ denotes reference values and ρ_∞ and c_∞ have the same meaning as ρ_L and c as used in Sec. I. The result shown in Fig. 8 has been obtained with this formulation in terms of the enthalpy. Use of the pressure as in (2) gives results that are indistinguishable if plotted on the same graph, but that are, nevertheless, somewhat different. For example, the pressure maxima shown in Fig. 8 have the values 140, 264, 352, and 490, while the corresponding values obtained by using Eq. (20) are 160, 280, 330, and 450.

As another example, we present in Fig. 9 a bifurcation diagram of the bubble radius sampled every 2π dimensionless time units for the same case of a 50-μm bubble driven at $\omega/\omega_0 = 0.8$ and a slowly increasing driving pressure amplitude. After steady state was reached at $\epsilon = 1.5$, the pressure was increased linearly at a rate of 0.001 per cycle up to $\epsilon = 1.9$ and then at a rate of 0.0001 per cycle. Two subharmonic bifurcations occur at $\epsilon \simeq 1.75$ and 2.03. These are followed by a third barely distinguishable bifurcation, a seemingly chaotic response, and a return to subharmonic oscillations with further bifurcations and chaos. It is likely that an even slower ramping of the driving pressure would give a better resolution of these features. To explore the nature of the large-amplitude chaotic response, we calculated 1500 cycles with a constant forcing of $\epsilon = 2.5$ and constructed the Poincaré maps in Fig. 10(a)–(c), in which the internal pressure is plotted against the radius and the radial velocity. These graphs confirm the chaotic nature of the bubble's response in these conditions. In all these calculations, the nu-
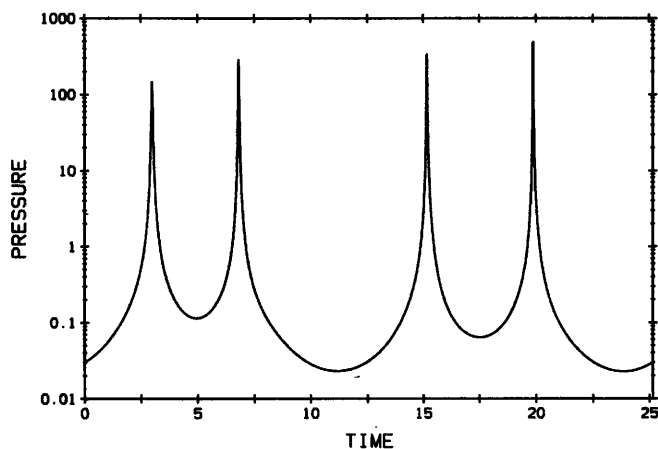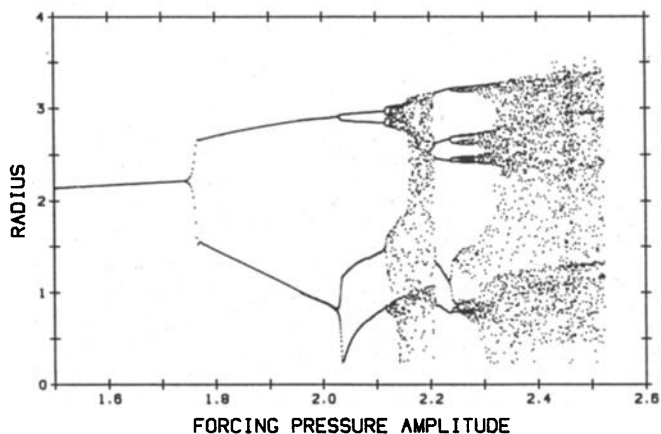

FIG. 8. Internal pressure versus time during the 30th–33rd cycles of the driving pressure for a 50-μm-radius air bubble in water driven at $\omega/\omega_0 = 0.8$ and a forcing $\epsilon = 2.05$. The oscillations have undergone two subharmonic bifurcations and now have period four. This result was obtained with the adaptive 20-term Galerkin–Chebyshev method and the Keller equation (37) in terms of the enthalpy.

FIG. 9. Bifurcation diagram of the bubble radius sampled every 2π dimensionless time units for a 50-μm-radius air bubble in water driven by a slowly increasing pressure field.
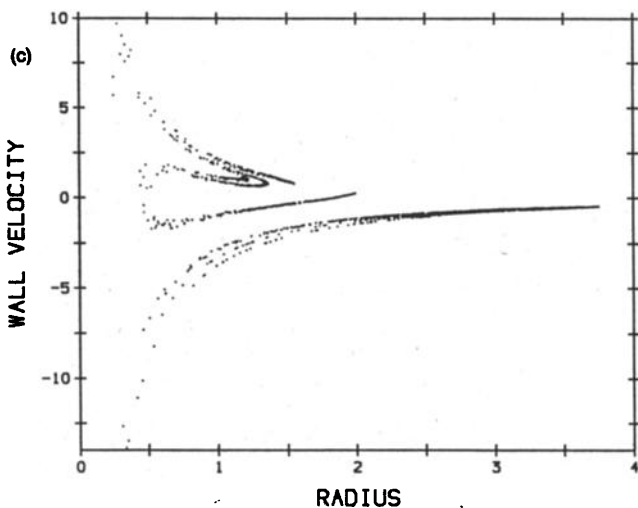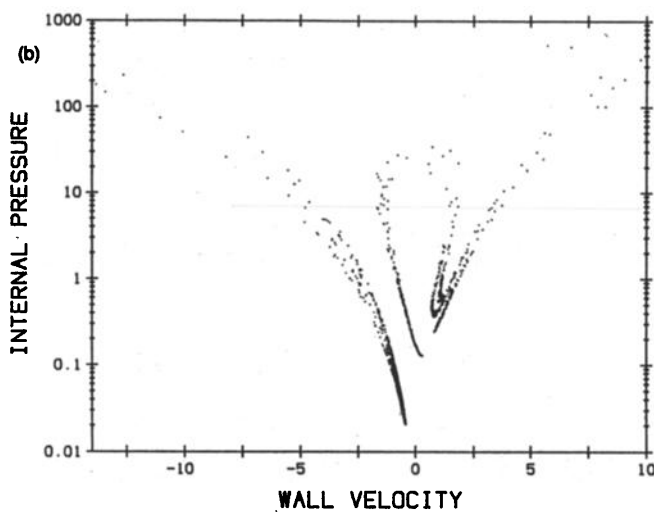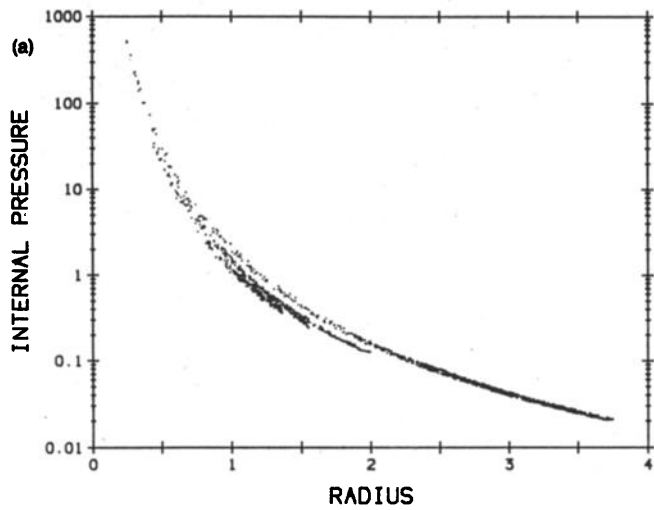
FIG. 10.(a)–(c) Poincaré plots of the internal pressure (logarithmic scale) versus radius and radial velocity sampled every 2π dimensionless time units for $\epsilon = 2.5$ for the same case as in Fig. 9.

merical method used was the adaptive 20-term Galerkin expansion with the radial equation (37) based on the enthalpy.

Earlier studies devoted to the analysis of the chaotic response of oscillating bubbles have employed a polytropic pressure–volume relationship of the type[10,11]

$$p = p_0 (R_0/R)^{3\kappa}, \qquad (40)$$

where $1 \leqslant \kappa \leqslant \gamma$. It is, therefore, interesting to compare the results given by our model with those that are derived from this simple assumption. We show in Figs. 11 and 12 the bifurcation diagrams obtained by use of Eq. (40) with $\kappa = 1.4$ (adiabatic behavior) and $\kappa = 1.2133$, which is the value of the polytropic index given by linear theory.[4,19] These graphs are to be compared with the results of Fig. 9. The differences are so great as to cast serious doubt on the validity of the polytropic approximation.

In the study of chaotic behavior, the use of a variable number of terms in the Galerkin expansion may appear rather questionable in view of the sensitive dependence of the chaotic response upon the detailed form of the equations. For this reason, we have compared the attractor of Fig. 10 with the same attractor as computed with a fixed 20-term expansion. The two attractors were found to be nearly indistinguishable. From this finding, it seems reasonable to conclude that the present adaptive technique does not introduce greater errors than those arising, for instance, from truncation.

V. LEGENDRE POLYNOMIALS

The Galerkin and collocation procedures implemented above with Chebyshev polynomials have also been tested with Legendre polynomials. For the Galerkin method, we have used the shifted polynomials

$$\phi_n = P_{2n} - P_0,$$

while, for the collocation method, we have used the regular polynomials $\phi_n = P_{2n}$. Other than the use of a different set of polynomials, and, therefore, different recurrence relations
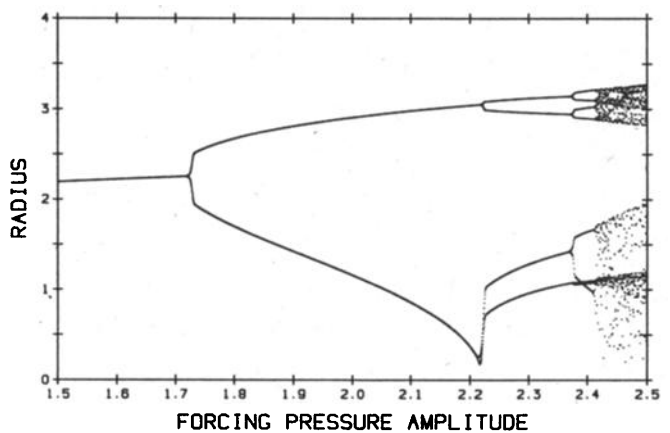

FIG. 11. Bifurcation diagram of the bubble radius sampled every 2π dimensionless time units for a 50-μm-radius air bubble in water driven by a slowly increasing pressure field. The internal pressure is given by the polytropic relation (40) with $\kappa = 1.4$.

FIG. 12. Bifurcation diagram of the bubble radius sampled every 2π dimensionless time units for a 50-μm-radius air bubble in water driven by a slowly increasing pressure field. The internal pressur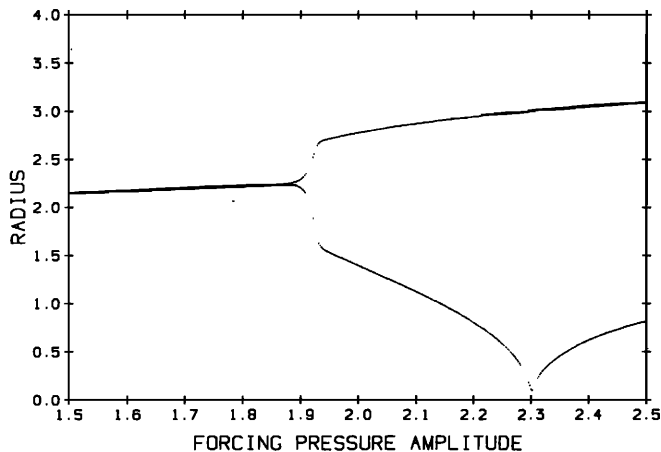e is given by the polytropic relation (40) with $\kappa = 1.2133$. This is the value of the polytropic index appropriate for linear oscillations.
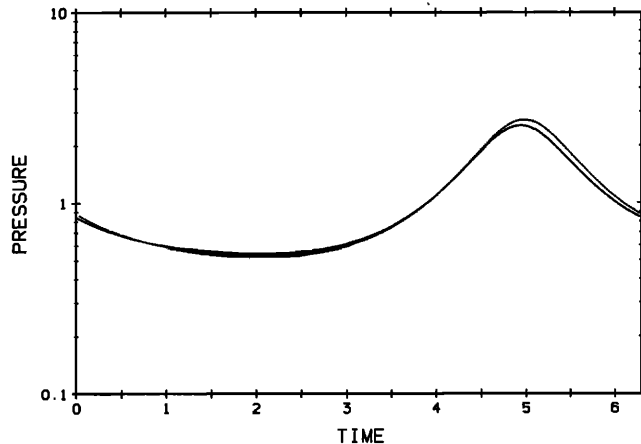

FIG. 13. The internal pressure during the 20th cycle of oscillation of a 10-μm-radius bubble driven at $\omega/\omega_0 = 0.8$ and a pressure amplitude of $\epsilon = 0.3$. The solid line shows the two very nearly coincident results given by the fixed 4-term Galerkin–Chebyshev method and the 101 nodes, 1000 time steps finite-difference calculation. The dotted line has been obtained with a fixed 7-term Galerkin–Legendre method.

and a different scalar product, the method of calculation is exactly the same as explained above. We do not give any detailed formulas because the Legendre polynomials converge much more slowly than the Chebyshev ones and therefore, for the same computational effort, give poorer results. As an example, we show in Fig. 13 the 20th oscillation of the same 10-μm bubble considered in the previous section, but driven at a much lower pressure amplitude, $\epsilon = 0.3$. The results of a finite-difference, 101 nodes and 1000 time steps, calculation and a fixed 4-term Chebyshev–Galerkin calculation superpose on the solid line, thus proving the accuracy of these relatively coarse calculations in this case of low forcing. The dotted line shows the result obtained with a 7-term Legendre expansion, which required eight times longer to run, but exhibits some residual error.

VI. AN ALTERNATIVE APPROACH

As already remarked in Sec. I, an alternative approach to the calculation of the temperature field in the bubble may be based on the equation of continuity and the equation of state of the gas which, in terms of the dimensionless quantities defined in (10), is simply

$$p = \rho T. \tag{41}$$

Here, the density ρ has been nondimensionalized with respect to its undisturbed value corresponding to the pressure p_0 and temperature T_∞. By use of the velocity field (4) and the normalized radial variable y defined by (8), it is readily shown that the continuity equation may be written as

$$\frac{\partial}{\partial t}(R^3 \rho) - \frac{1}{y^2}\frac{\partial}{\partial y}\left[y^2 R\chi\left(D\frac{\partial p}{\partial y} - y\frac{\rho}{p^2}\frac{\partial p}{\partial y}\bigg|_{y=1}\right)\right] = 0. \tag{42}$$

The thermal diffusivity is given by (19), which now reads

$$D = (1/\rho)[\alpha(p/\rho) + 1 - \alpha]. \tag{43}$$

Upon introduction of the variable

$$\psi = y\rho, \tag{44}$$

Eq. (42) becomes

$$\frac{\partial \psi}{\partial t} = \frac{\chi}{R^2}\left[D\frac{\partial^2 \psi}{\partial y^2} - \frac{1}{p^2}\left(2\psi + y\frac{\partial \psi}{\partial y}\right)[\psi]|_1 \right.$$
$$\left. + \left(\frac{\partial \psi}{\partial y} - \frac{\psi}{y}\right)\frac{\partial D}{\partial y}\right] - \frac{3U}{R}\psi, \tag{45}$$

where

$$[\psi]|_1 = \frac{\partial \psi}{\partial y}\bigg|_{y=1} - \psi|_{y=1}. \tag{46}$$

The boundary condition at $y = 1$ is, from (41) and (44),

$$\psi(1,t) = p, \tag{47}$$

while at $y = 0$ the condition $\partial p/\partial y = 0$ translates into

$$\frac{\partial^2 \psi}{\partial y^2} = 0. \tag{48}$$

In terms of ψ, the equation for the total mass (22) reads

$$m = 3R^3\int_0^1 y\psi\, dy. \tag{49}$$

Our original intent in using this formulation was to make use of the family of Jacobi polynomials orthogonal on the interval [0,1] with respect to the weight function y. In this way, the first term of the series expansion of ψ would have carried the entire mass, which would have been conserved exactly. This plan was unsuccessful because instabilities set in already at forcings as low as 0.5–0.6. Since the Legendre polynomials P_1 equal y, mass would also be conserved exactly by expanding ψ in a series of Legendre polynomials. We tried this approach, but it failed for the same reason although, where the method is stable, fewer terms are needed than with the Jacobi polynomials. Finally, we tried an implicit finite-difference scheme based on (45) with and without upwinding of the convective terms, and again found instabilities. The conclusion is that the formulation based on the temperaturelike variable τ is far more easily amenable to a numerical solution than a formulation based on the density.

VII. SUMMARY AND CONCLUSIONS

We have studied a number of techniques for the numerical integration of a detailed model of gas-bubble oscillations. An adaptive spectral method using a variable number of terms has been found to be the most efficient of the techniques considered, cutting integration times by an order of magnitude with respect to the earlier finite-difference method.

As an example of the results obtainable in this way, we have studied the regime of chaotic oscillations in a particular case, and we have compared the results with those of earlier investigations. The differences that have been encountered are so profound that the results given by the simpler models used by previous investigators at best bear only the vaguest resemblance with those of our more precise approach. This finding is in agreement with our previous conclusions[4] and underscores the importance of a precise calculation of the internal pressure in the simulation of the oscillations of gas bubbles.

ACKNOWLEDGMENT

APPENDIX

The value of the scalar product introduced in Sec. II is

$$(\phi_n,\phi_m) = \int_{-1}^{1} \phi_n(y)\phi_m(y)\frac{1}{\sqrt{1-y^2}}\,dy = \frac{\pi}{2}\delta_{nm} + \pi.$$

The diagonal terms of the matrix of the linear system (31) are, therefore, all equal to $3\pi/2$, while all the off-diagonal terms are equal to π. The inverse of such a matrix is readily calculated and has all the diagonal terms equal to $2(2N-1)/(2N+1)\pi$, while the off-diagonal terms are all equal to $-4/(2N+1)\pi$.

The Gauss points y_j and weights w_j for the numerical integration appearing in (30) are

$$y_j = \cos[\pi(2j-1)/4N], \quad w_j = \pi/2N,$$

with $j = 1,2,...,N$.

We now give the relations that are needed to evaluate the spatial derivatives of τ in Eqs. (28) and (29). For the coefficients e_n of the first derivative, we have

$$e_n = 4\sum_{k=n}^{N} ka_k,$$

while, for the calculation of the Laplacian according to (28),

$$d_n = b_n + 2g_n,$$

where

$$\nabla^2\tau = \frac{\partial^2\tau}{\partial y^2} + \frac{2}{y}\frac{\partial\tau}{\partial y} = \sum_{n=0}^{N} b_n T_{2n} + 2\sum_{n=0}^{N} g_n T_{2n}$$

and

$$f_n g_n = 8\sum_{\substack{k=n+1 \\ k+n=\text{odd}}}^{N} ka_k,$$

$$f_n b_n - b_{n+1} = 2(2n+1)e_{n+1},$$

and $b_N = 0$. Here, we have defined

$$f_n = \begin{cases} 0 & \text{if } n\leqslant 0, \\ 2 & \text{if } n = 0, \\ 1 & \text{if } n > 1. \end{cases}$$

If we set

$$y\frac{\partial\tau_N}{\partial y} = \sum_{n=0}^{N} c_n T_{2n},$$

the scalar product of the linear part of the operator with the basis functions ϕ_k has the form

$$(\phi_k,\mathsf{L}\tau_N) = (\pi/2)(c_k - 2c_0),$$

where

$$c_k = \tfrac{1}{2}(f_k e_k + e_{k+1}).$$

The above expressions are general. As mentioned in the text, a very simple 4-term version of the Galerkin method has a rather wide range of applicability, and we shall therefore present, in detail, the formulas for this case. The matrix of scalar products (ϕ_k,ϕ_n) appearing in the left-hand side of (31), in this case, is

$$\pi\begin{pmatrix} \frac{3}{2} & 1 & 1 & 1 \\ 1 & \frac{3}{2} & 1 & 1 \\ 1 & 1 & \frac{3}{2} & 1 \\ 1 & 1 & 1 & \frac{3}{2} \end{pmatrix}. \tag{A1}$$

In obtaining from (31) explicit relations for the derivatives of the expansion coefficients a_n, the inverse of this matrix is needed. It is

$$\frac{1}{9\pi}\begin{pmatrix} 14 & -4 & -4 & -4 \\ -4 & 14 & -4 & -4 \\ -4 & -4 & 14 & -4 \\ -4 & -4 & -4 & 14 \end{pmatrix}. \tag{A2}$$

From the previous expressions, we have the following explicit relations for the coefficients appearing in (27)–(29):

$$e_1 = 4a_1 + 8a_2 + 12a_3 + 16a_4,$$

$$e_2 = 8a_2 + 12a_3 + 16a_4,$$

$$e_3 = 12a_3 + 16a_4, \quad e_4 = 16a_4,$$

$$d_0 = 12a_1 + 32a_2 + 132a_3 + 256a_4,$$

$$d_1 = 80a_2 + 192a_3 + 544a_4,$$

$$d_2 = 168a_3 + 384a_4, \quad d_3 = 288a_4, \quad d_4 = 0,$$

$$c_0 = 2a_1 + 4a_2 + 6a_3 + 8a_4,$$

$$c_1 = 2a_1 + 8a_2 + 12a_3 + 16a_4,$$

$$c_2 = 4a_2 + 12a_3 + 16a_4, \quad c_3 = 6a_3 + 16a_4, \quad c_4 = 8a_4.$$

The Gauss points for this case are $\cos(\pi/16)$, $\cos(3\pi/16)$, $\cos(5\pi/16)$, and $\cos(7\pi/16)$ with equal weights $\pi/8$.

[1] R. I. Nigmatulin and N. S. Khabeev, Fluid Dyn. USSR 12, 867 (1977).

[2] F. B. Nagiev and N. S. Khabeev, Sov. Phys. Acoust. 25, 148 (1979).

[3] R. I. Nigmatulin, N. S. Khabeev, and F. B. Nagiev, Int. J. Heat Mass Transfer 24, 1033 (1981).

[4] A. Prosperetti, L. A. Crum, and K. W. Commander, J. Acoust. Soc. Am. 83, 502 (1988).

[5] B. E. Noltingk and E. A. Neppiras, Proc. R. Phys. Soc. London Ser. B 63, 674 (1950).

[6]H. G. Flynn, "Physics of Acoustic Cavitation in Liquids," in *Physical Acoustics*, edited by W. P. Mason (Academic, New York, 1964), Vol. 1, Part B, pp. 58–172.

[7]W. Lauterborn, J. Acoust. Soc. Am. **57**, 1379 (1976).

[8]A. Prosperetti, J. Acoust. Soc. Am. **56**, 878 (1974).

[9]R. E. Apfel, J. Acoust. Soc. Am. **69**, 1624 (1981).

[10]W. Lauterborn and E. Suchla, Phys. Rev. Lett. **53**, 2304 (1984).

[11]P. Smereka, B. Birnir, and S. Banerjee, Phys. Fluids **30**, 3342 (1987).

[12]M. J. Tan and S. G. Bankoff, Phys. Fluids **27**, 1362 (1984).

[13]R. Omta, J. Acoust. Soc. Am. **82**, 1018 (1987).

[14]J. B. Keller and I. I. Kolodner, J. Appl. Phys. **27**, 1152 (1956).

[15]J. B. Keller and M. J. Miksis, J. Acoust. Soc. Am. **68**, 628 (1980).

[16]A. Prosperetti and A. Lezzi, J. Fluid Mech. **168**, 457 (1986).

[17]D. Gottlieb and S. A. Orszag, *Numerical Analysis of Spectral Methods: Theory and Applications* (SIAM-CBMS, Philadelphia, 1977).

[18]C. Canuto, M. Y. Hussaini, A. Quarteroni, and T. A. Zang, *Spectral Methods in Fluid Dynamics* (Springer, New York, 1988).

[19]A. Prosperetti, Ultrasonics **22**, 69 (1984).